Optics & Laser Technology 182 (2025) 112241

Contents lists available at ScienceDirect

Optics and Laser Technology

journal homepage: www.elsevier.com/locate/optlastec

Full length article

Structural, Morphological, and optical analysis for $CuFeS_2$ nanoparticles prepared by pulsed laser ablation technique in ethanol

R. Onsi *, M. Nabil *, S. Abdallah, S. Negm, k. Easawi

Basic Engineering Sciences Department, Faculty of Engineering (shoubra), Benha University, Egypt

ARTICLE INFO

Keywords:
Copper iron sulfide
Laser ablation
Optical conductivity
Urbach energy
Steepness parameter
Electron–phonon interaction

ABSTRACT

In this work, we successfully synthesized different sizes of copper iron sulfide ($CuFeS_2$) nanoparticles (NPs) using a pulsed laser ablation technique in liquid (PLAL) with different ablation times. We evaluated the structure of $CuFeS_2$ NPs using experimental results obtained from high resolution transmission electron microscope (HR-TEM), scanning electron microscope (SEM), energy dispersive x-ray (EDX), Fourier transform infrared (FTIR), Raman spectroscopy, and UV–Vis spectroscopy. TEM images revealed that the $CuFeS_2$ nanoparticles are shaped like spheres and have an average size of 17.9 to 44.2 nm with ablation time ranging from 10 to 50 min. We used EDX and mapping to examine the surface morphology and the percentage distribution of each element in the prepared samples. FTIR measurements confirm the bonds between elements. Raman spectroscopy evaluates the molecular structure, the molecule's geometry, and even its symmetry. According to the samples' UV–vis spectra, the optical parameters were looked at. These included the optical absorption coefficient ($\boldsymbol{\alpha}$), band gap energy ($\mathbf{E_g}$), Urbach energy ($\mathbf{E_u}$), refractive index ($\mathbf{n}$), extinction coefficient ($\mathbf{k}$), skin depth ($\boldsymbol{\delta}$), optical conductivity ($\boldsymbol{\sigma_{opt}}$), and dielectric constants (ε', ε''). We found that as the particle size of $CuFeS_2$ NPs increases, the direct optical band gap decreases from 2.54 to 1.915 eV, while the Urbach energy increases from 1.64 to 3.11 eV. While the Urbach energy increases, the electron–phonon interaction ($\boldsymbol{E_{e-p}}$) increases from 42.46 to 80.22, and the steepness parameter ($\boldsymbol{\sigma}$) decreases from 0.0157 to 0.00831. Furthermore, we observed an increase in the refractive index, extinction coefficient, optical dielectric, and optical conductivity of $CuFeS_2$ NPs. The prepared $CuFeS_2$ NPs have the potential to be crucial in optoelectronic and energy storage applications.

1. Introduction

Transition metal oxides (TMOs) have received attention because of their special characteristics, but they have low electrical conductivity. Thus, scientists attempt to investigate alternative electrode materials that may possess the essential qualities of a desirable electrode material, such as stability, environmental friendliness, and electrical conductivity [1-3]. Because sulfur is more electronegative than oxygen, researchers are drawn to transition metal sulfides (TMSs) since they can successfully replace oxygen in compounds and create compounds with better ionic diffusivity [4-6]. Besides having higher electrical conductivity than oxides, sulfides are less expensive and have superior electrochemical performance [7,8]. There are numerous applications that can use TMSs, like supercapacitors, batteries, and solar cells, to improve the performance of the device [9-13]. $CuFeS_2$ is a tetragonal element belonging to the I-III-VI family of elements [14,15]. Researchers want to study them since they are abundant and have little toxicity. A common n-type semiconductor with a relatively narrow band gap is $CuFeS_2$ which exhibits superior photoelectric and magnetic properties, making it a favorable material for solar cells [16-18]. Researchers have published numerous studies on the synthesis of $CuFeS_2$ NPs using various solutions, including hydrothermal, chemical bath, solvothermal hot injection, and one-pot methods. The manufacturing of $CuFeS_2$/graphene composite electrodes is complex and requires a binder, which increases costs and decreases performance [19-21]. Lokhande et al. used a single-step hydrothermal process without a binder to prepare $CuFeS_2$ NPs. The creation of nanoparticles using pulsed laser ablation in a liquid medium (**PLAL**) has drawn a lot of interest as a unique method for producing nanoparticles. The unique physical characteristics of these nanoparticles, along with their dramatic Plasmon absorption peak in the visible region, make them highly desirable for a variety of biophysical, biochemical, and biotechnological applications. In brief, this technique involves focusing a laser beam on a large target and removing the material surface. A delayed mass, or plume, forms beneath the liquid and

* Corresponding author.
E-mail addresses: romany.onsi@yahoo.com (R. Onsi), mohammed_diab35@yahoo.com (M. Nabil).

https://doi.org/10.1016/j.optlastec.2024.112241
Received 18 May 2024; Received in revised form 19 October 2024; Accepted 29 November 2024
Available online 2 December 2024
0030-3992/Published by Elsevier Ltd.

releases a variety of species, among them nanoparticles. The liquid environment surrounding the ablated plume creates nanoparticles through the rapid condensation of molten bubbles, collisions among plume species, or the nucleation of clusters from free atoms [23,24]. The three main benefits of using the **PLAL** method to manufacture nanoparticles are their excellent stability, relative ease of use, and lack of need for chemical reagents during the final manufacturing step [22]. Therefore, we used the laser ablation technique in the preparation of $CuFeS_2$ NPs in ethanol. In this work, we successfully synthesize different sizes of $CuFeS_2$ NPs in ethanol using the pulsed laser ablation technique. HR-TEM, EDX, FTIR, and Raman spectroscopy were measured to analyze the obtained samples. We also estimated the optical properties of $CuFeS_2$ NPs, including the absorption coefficient, band gap energy, Urbach energy, steepness parameter, and the strength of the electron–phonon interaction.

2. Experimental details

2.1. Preparation of $CuFeS_2$ nanoparticles using PLAL

We purchased the alloy target, which included copper, iron, and sulfur, from Sammlung VON and the ethanol from Sigma Aldrich. Fig. 1 schematically represents the experimental setup. The experimental setup involved focusing a lens with a focal length of 20 cm on the beam of a pulsed Q-Switched Nd:YAG laser with a wavelength of 1064 nm, a pulse duration of 8 ns, and a repetition rate of 10 Hz on the target's surface (purity: 99.99 % from Sigma Aldrich). The solid target, $CuFeS_2$, had dimensions of 2 by 2 cm and a thickness of 2 mm. We placed it in a glass vessel at the bottom, which contained 20 ml of ethanol.

After cleaning the target for 30 min with ethanol and distilled water to remove organic contaminants, we mounted it 16 mm below the liquid surface. We first cleaned the target using the ultrasonic bath. The laser beam focused on the target with ablation times ranging from 10 to 50 min, using a laser power of 480 mj. The liquid was initially colorless, but it soon started to turn yellow and eventually brown. The deeper colors of the solutions indicate a larger concentration of $CuFeS_2$ NPs. When the laser beam strikes a material, its surface transmits the energy it carries to the highest layers of the substance. The result is a rise in temperature that surpasses the melting point [25,26]. The high power in a few nanosecond pulses causes surface melting, vaporization, and material ejection, as the energy density exceeds the material's ablation threshold. During this process, the surface releases various species such as ions, molecules, and particles, which absorb incoming energy to form plasma [10–13]. The process in a liquid rapidly lowers the temperature of the plasma plume, leading to the formation of spherical nanoparticles.

2.2. Characterization techniques

We employed a lens with a focal length of 20 cm to concentrate a 1064 nm wavelength, 8 ns pulse duration, and 10 Hz repetition rate Nd:YAG (Quanta-Ray) laser on the target's surface. We used the (COHERENT-LASERMATE/D) power meter to measure the energy of the incident laser pulse. We determined the size distribution and form of the nanoparticles using a High-Resolution Transmission Electron Microscope (HRTEM) (JEM-2100). We analyzed the $CuFeS_2$ NPs sample's surface shape and elemental composition using the TEM (JEOL JEM-2010F) and EDX (Energy Dispersive X-ray Spectroscopy). We obtained the functional group organization of the $CuFeS_2$ nanocomposite using FTIR (Bruker ALPHA, Germany) and Raman Spectra (HORIBA-LABRAM HR EVO) in the range of 4000–400 cm^{-1}. We used a UV–Vis double-beam spectrometer of the JASCO V-670 type to examine the absorption spectra of the $CuFeS_2$ NPs in ethanol immediately after the ablation procedure.

3. Results and discussion

3.1. Structural and morphological investigation

3.1.1. HR-TEM analysis.

As shown in Fig. 2, we used HR-TEM analysis to determine the average particle size of $CuFeS_2$ NPs with different ablation times (10 min, 30 min, and 50 min), respectively. The estimated average size using different resolutions and the particle size distribution histogram of the produced NPs with a 10-minute ablation time was 17.9 nm, as shown in Fig. 2**(a)**; with increasing the ablation time to 30 and 50 min, the size increased to 35.2 nm and 44.2 nm, respectively, as shown in Fig. 2**(b and c)**.

The interaction of the generated nanoparticles with the laser light for longer ablation durations was the cause of this rise in particle size. By increasing ablation time, when the little particles contact one another, they squeeze and fuse together to form giant particles that take center stage for a while [27]. Longer ablation periods result in the formation of larger particles, while the narrower particle distribution suggests no significant aggregation. Fig. 2**a(l), 2b(l), and 2c(l)**, respectively, display the Selected Area of Electron Diffraction (SAED) pattern for the prepared samples with different ablation times (10, 30, and 50 min). This demonstrates that the processed samples are polycrystalline based on the ring pattern with intense spots.

3.1.2. SEM micrographs, EDX, and mapping analysis

We used the SEM analysis to study the structure of the $CuFeS_2$ NPs with different ablation times (10 min, 30 min, and 50 min), respectively,

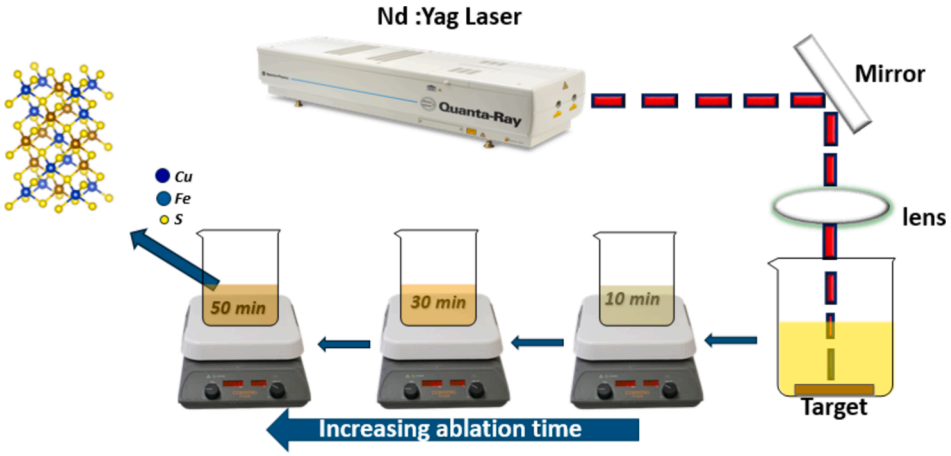

Fig. 1. Schematic diagram for $CuFeS_2$ NPs Prepared by Pulsed Laser Ablation Technique in Ethanol.

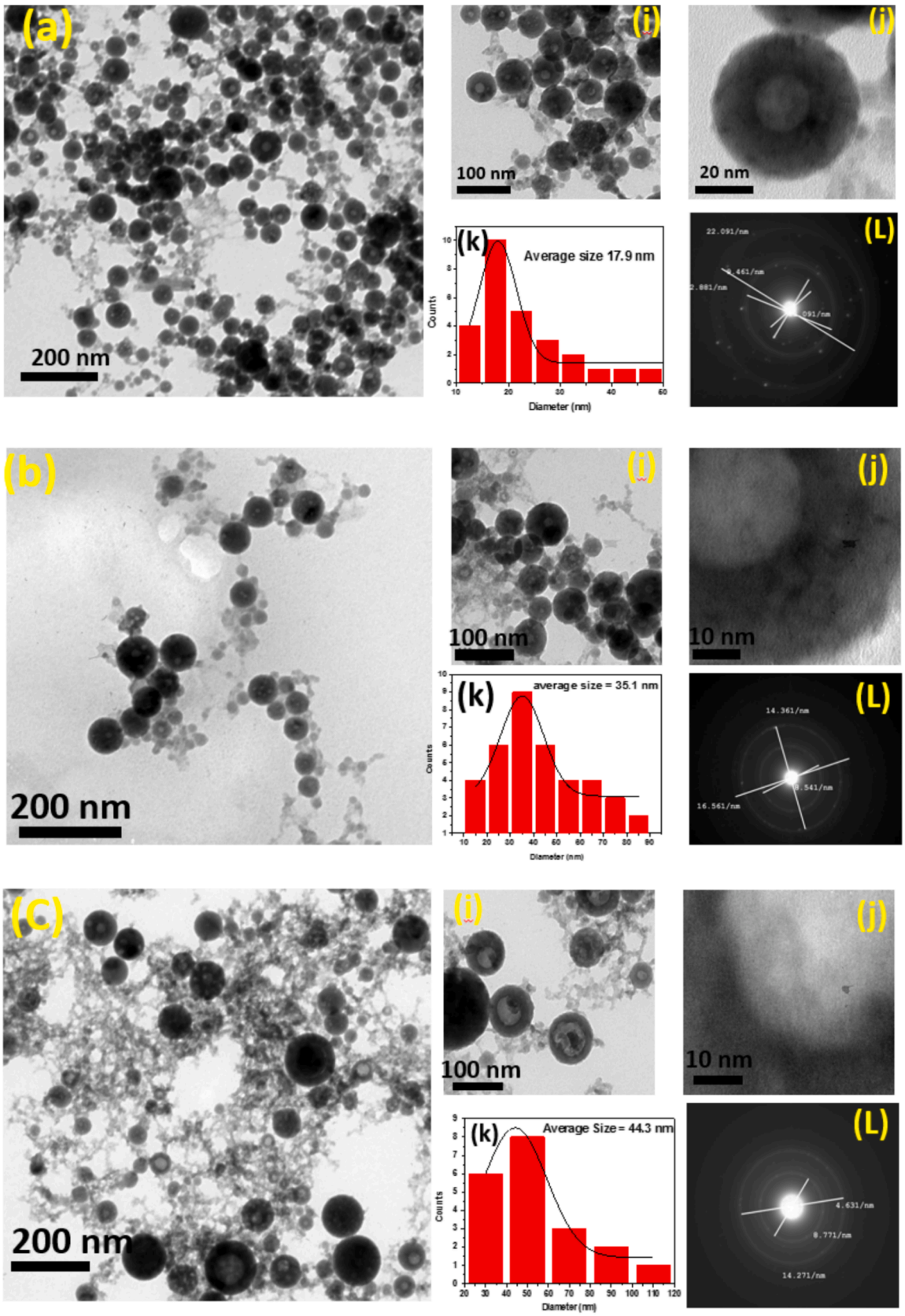

Fig. 2. (a-k), (b-k), and (c-k) HR-TEM images and particle size distribution histogram of $CuFeS_2$ NPs with 10 min, 30 min, and 50 min of ablation time, respectively. a (l), b(l), and c(l) show the SAED pattern for the prepared samples with different ablation times of 10, 30 and 50 min, respectively.

as shown in Fig. 3**(a–c)**. We found that $CuFeS_2$ NPs have a spherical shape and nanometer-scale particle size.

Energy dispersive x-ray spectroscopy (EDX) and mapping are shown in Fig. 3**(a1, b1, and c1)**. The obtained samples' elemental compositions are determined by EDX and mapping, which also display an atomically consistent distribution. By using a laser ablation approach, the elemental mapping verifies that Fe, Cu, and S are present in the three samples of $CuFeS_2$ (chalcopyrite).

3.1.3. *Raman spectroscopy*

Raman spectroscopy can determine the molecular structure and assess the molecule's geometry and even symmetry. The Raman spectrum of the $CuFeS_2$ NPs sample is shown in Fig. 4**(a).** It displays different peaks in the range of 200–700 cm^{-1} at wavenumbers such as 216, 275, 385, 473, and 580 cm^{-1}. The characteristic peaks at 275, 473 cm^{-1}, and 385 cm^{-1} of $CuFeS_2$ NPs correspond to Cu—S and Fe—S bonds, respectively [1]. However, under these conditions, a peak associated with sulfur (216 cm^{-1}) becomes more visible.

Chalcopyrite is a mineral with a complicated layer structure that includes covalently bonded sulfur dimers between layers and solitary sulfur atoms within layers. Notably, the symmetric S—S stretching band and lattice vibration are also shown by the Raman spectrum's peaks at 275 and 473 cm^{-1}. Furthermore, the data given indicates that $CuFeS_2$ NPs have four characteristic peaks, which are 275, 323, 385, and 473

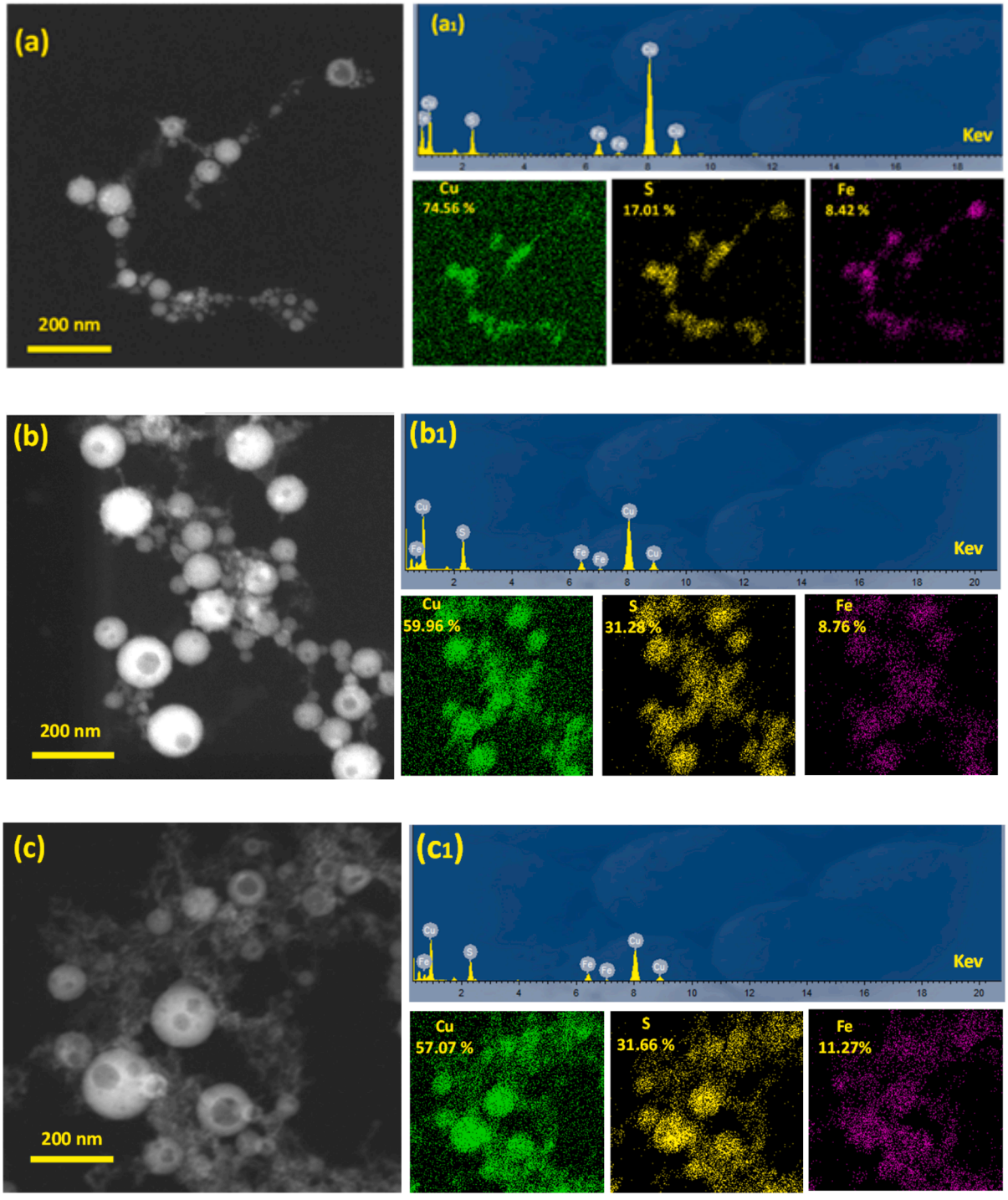

Fig. 3. SEM, EDX, and Mapping for $CuFeS_2$ nanoparticles at different ablation times (a) 10 min (b) 30 min (c) 50 min.

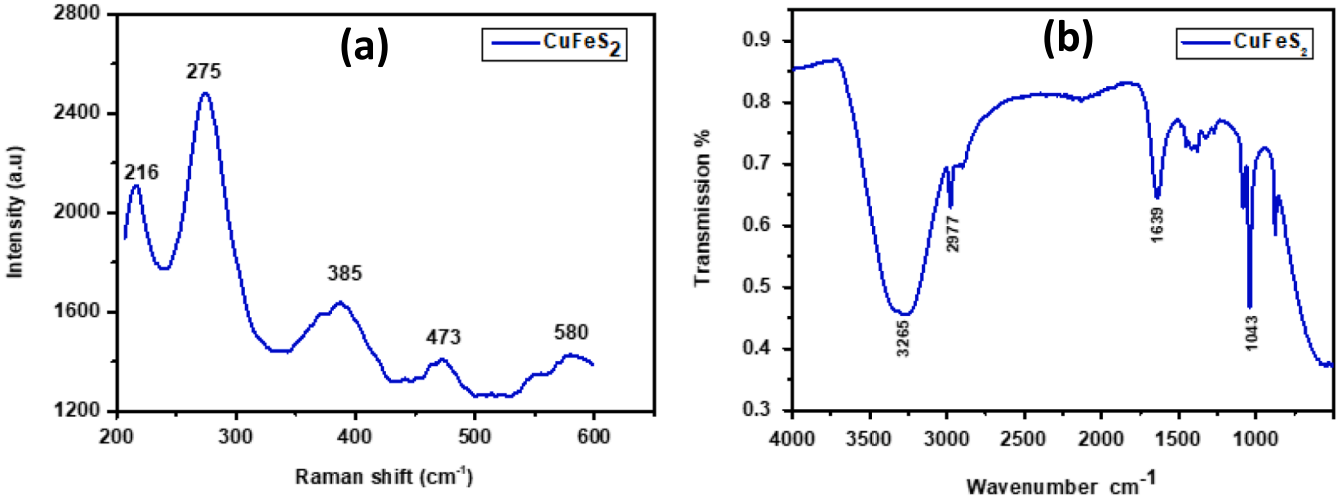

Fig. 4. (a) Raman Spectroscopy (b) FTIR for $CuFeS_2$ Nanoparticles at 30 min ablation time.

cm^{-1} [16].

3.1.4. Fourier transform infrared (FT-IR) spectroscopy analysis

FTIR is a useful tool for learning more about how raw materials respond and how products are structured. Fig. 4**(b)** shows three peaks located at 1043, 1639, and 3265 cm^{-1}, which corresponded to the C═S stretching and O—H bending vibrations, respectively. We attribute the O—H bending in the produced $CuFeS_2$ NPs to their preparation in ethanol, known to contain O—H groups. The C═S stretching in the prepared $CuFeS_2$ NPs might be derived from the L-cysteine precursor [28].

3.2. Optical characterization.

3.2.1. Absorption, Transmission, and reflectance studies.

Fig. 5**(a)** displays the absorption spectra for $CuFeS_2$ NPs prepared at

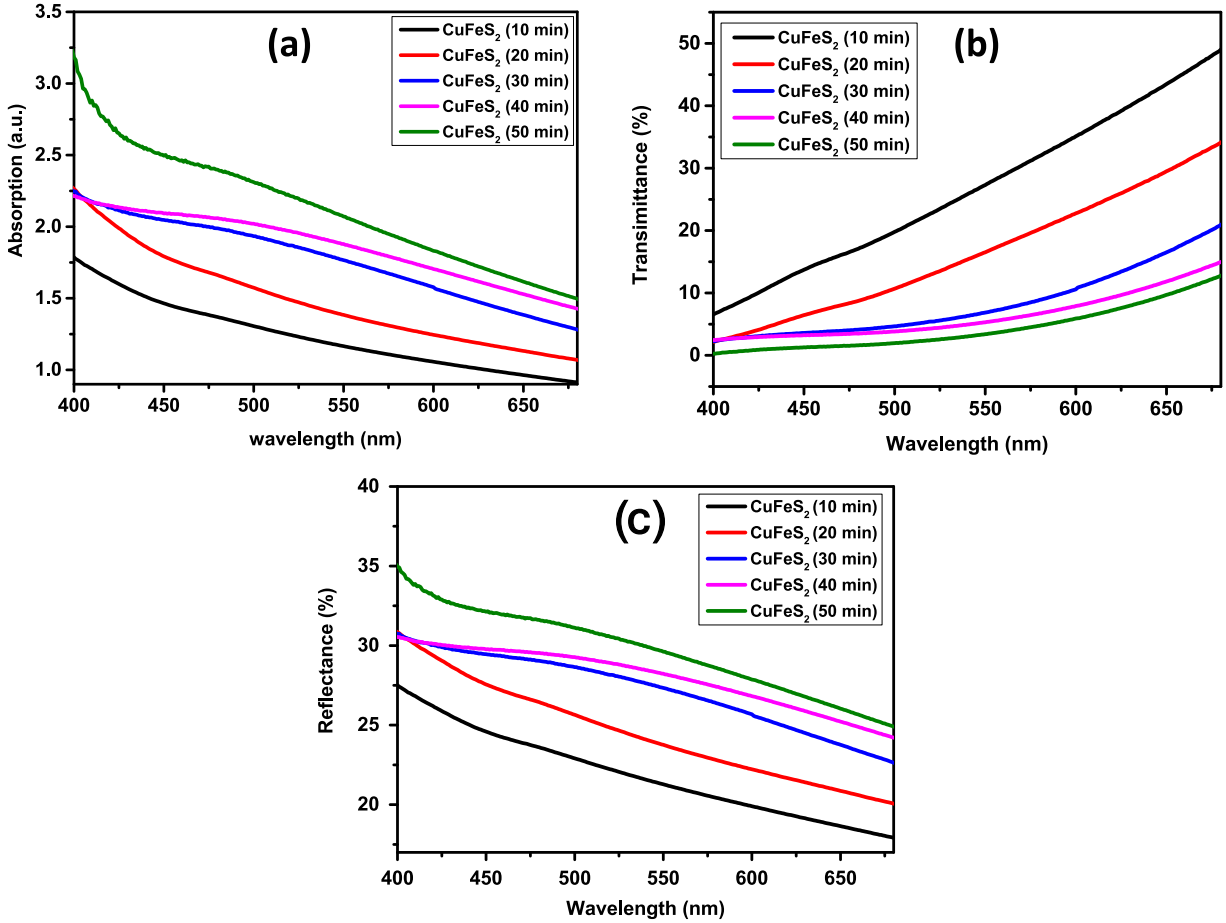

Fig. 5. (a) Absorption spectra; (b) Transmission spectra; (c) Reflectance spectra for $CuFeS_2$ nanoparticles prepared at different ablation times.

various ablation times, covering wavelengths from 400 to 700 nm. It was evident that the absorbance of $CuFeS_2$ NPs increased as the ablation time increased, and the absorption edge shifted toward higher wavelengths, exhibiting a red shift. This indicates the increase in the particle size for $CuFeS_2$ NPs, which the quantum confinement effect is responsible for. The peak intensity of the spectra increases as the volume percentage and concentration of $CuFeS_2$ NPs in the liquid increase. Fig. 5**(b)** depicts the transmission spectrum of $CuFeS_2$ NPs at various ablation times. The transmission decreases with an increase in the ablation time due to particle size increases.

The optical reflectance was found to have the opposite behavior of the optical transmittance, as shown in Fig. 5**(c)**. Additionally, the wavelength at which the maximum reflectance value occurred roughly corresponds to the absorption edge.

3.2.2. Optical absorption coefficient (α), optical band gap, and Urbach energy

The following equation can determine the absorption coefficient (**α**) for the $CuFeS_2$ NPs [26]:

$$\alpha = 2.303A/t \tag{1}$$

where (**t**) is the prepared sample thickness and (**A**) is its absorbance. The variation in the absorption coefficient (**α**) of $CuFeS_2$ NPs as a function of photon energy (**h**) is shown in Fig. 6**(a)** The absorption coefficient obviously drops exponentially with wavelength. This behavior, which is common in many semiconductors, could be caused by several things, such as electric fields inside the crystal, strain from imperfections that cause the lattice to deform, and the inelastic spreading of charge carriers by phonons. The absorption coefficient (**α**) for the different samples has a broad band in the visible spectrum and a higher peak near 400 nm and 540 nm [29]. The key element in optical absorption is electronic transitions.

Tauc's equation can express the selection principles that govern these transitions:

$$\alpha h\upsilon = A\left(h\upsilon - E_g\right)^m \tag{2}$$

where **m** is the transition power factor, **A** is a constant, and **α** is the absorption coefficient. The transition power factor (**m**) takes the values of (0.5 and 2) for allowed direct and indirect band gaps and (1.5 and 3) for forbidden direct and indirect transitions [30]. The tauc-plot curve of $(\alpha h\upsilon)^2$ values against (**hυ**) as seen in Fig. 6**(b)** determines the actual

Table 1
Particle size, bandgap energy, Urbach energy, steepness parameters, and electron–phonon interaction for $CuFeS_2$ nanoparticles at different ablation times.

Ablation Time (min)	Particle Size (nm)	Band Gap Energy (ev)	Urbach Energy (E_U) (ev)	Steepness Parameter (σ)	Electron –Phonon Interaction
10	**17.9**	**2.54**	**1.64**	**0.0157**	**42.46**
20	**25.12**	**2.348**	**1.92**	**0.0134**	**49.75**
30	**35.2**	**2.238**	**2.34**	**0.0110**	**60.6**
40	**39.3**	**2.11**	**2.71**	**0.00953**	**69.95**
50	**44.2**	**1.915**	**3.11**	**0.00831**	**80.22**

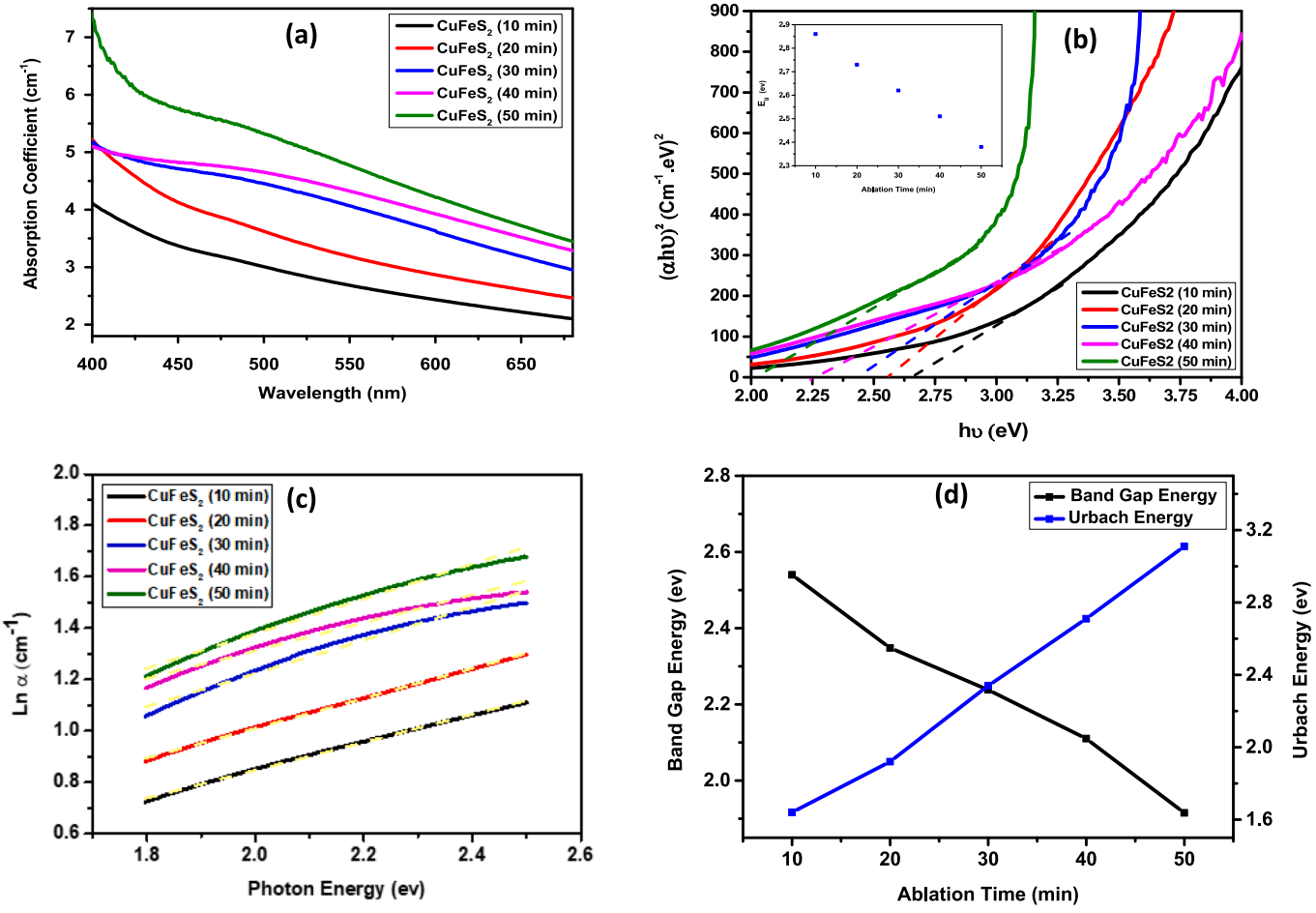

Fig. 6. (a) Absorption coefficient; (b) band gap energy; (c) ln (α) versus (hυ) to evaluate the Urbach energy; and (d) The variation of (E_g) and (E_u) with ablation time for $CuFeS_2$ samples.

value of the band gap. As shown in Fig. 6**(b)** and Table 1, the variation of the direct bandgap ($\mathbf{E_g}$) value decreased from 2.54 to 1.915 eV by increasing the ablation time from 10 to 50 min. We attribute this to the influence of the quantum confinement effect. This allows for the adjustment of these materials' band gaps for suitable opto-electronic applications [31]. Semiconducting materials' optical absorption spectra are crucial because they provide fundamental details about their composition and optical band gap. An exponential part known as the Urbach tail ($\mathbf{E_U}$) exists along the absorption coefficient curve and near the optical band edge.

Fig. 6**(c)** shows the graphical representation of ($\mathbf{ln\ (\alpha)}$) versus ($\mathbf{h}\ \nu$) in the range of the Urbach tail. Urbach energy ($\mathbf{E_U}$) is a parameter that represents the band tail of the localized states in the band gap. The ($\mathbf{E_U}$) can be obtained from the Urbach empirical relation [28].

$$Ln(\alpha) = ln\alpha o - (1/E_U)h\gamma \tag{3}$$

where (α_0) is a constant, (**h**) is Planck's constant, and (γ) is the frequency of radiation. For $CuFeS_2$ NPs with varying ablation times, this will result in a straight line with a slope equal to ($\mathbf{1/E_u}$) and an intercept y-axis in a portion equal to $\mathbf{ln\ \alpha_o}$. The calculated value of Urbach energy ($\mathbf{E_u}$) for $CuFeS_2$ NPs with different ablation times is tabulated in Table 1**.** The dependence of the band tail energy and the optical energy gap upon the different ablation times for prepared $CuFeS_2$ NPs can be illustrated in Fig. 6**(d).** It can be observed that the value of the band tail energy ($\mathbf{E_u}$) increased with increasing the ablation time, but the relation was not exactly linear. As seen in Fig. 6**(d)**, the behavior of the optical energy gap is contrary to the growing Urbach energy. The steepness parameter ($\boldsymbol{\sigma}$) can be evaluated from Urbach energy according to Eq. **(4)**. Table 1 contained the estimated values for this parameter.

$$\sigma = \frac{K_B.T_a}{E_U} \tag{4}$$

were, $\mathbf{K_B}$ Boltzmann constant, $\mathbf{T_a}$ absolute temperature. Additionally, the following relationship exists between the steepness parameter ($\boldsymbol{\sigma}$) and the strength of the electron–phonon interaction (E_{e-p}):

$$E_{e-p} = \frac{2}{3\sigma} \tag{5}$$

Therefore, it is possible to determine the values of the electron–phonon interaction strength (E_{e-p}), which are subsequently presented in Table 1. The dependence of the electron–phonon interaction and the steepness parameter on the ablation time is shown in Fig. 7**(a) and (b)**.

When the ablation time was increased, it was found that the values of the steepness parameter decreased and the values of the electron–phonon interaction increased, indicating that their relationship is inversely proportional [32,33].

3.2.3. The refractive index (n) and extinction coefficient (k)

The refractive index (**n**) and the extinction coefficient (**k**) are the two most important factors for optical applications. Using the reflectance (**R**) and absorption coefficient ($\boldsymbol{\alpha}$), these optical characteristics were calculated using the following formulas:

$$R = 1 - [T * exp(A)]^{1/2} \tag{6}$$

$$n = \frac{1+\sqrt{R}}{1-\sqrt{R}} \tag{7}$$

$$K = \frac{\alpha\lambda}{4\pi} \tag{8}$$

where **R** is the reflectance, **T** is the transmission, and **A** is the absorption. Examining the refractive index of optical materials is important because many optical phenomena depend on it and because it is intimately linked to the local field and electronic polarization of ions inside optical materials [30 34–36].

Fig. 8**(a)** illustrates the dependence of the refractive index on the wavelength of the incident light. When the ablation time increases, the value of **n** for all the prepared samples rises. The interaction of incident light with the prepared samples causes the refractive index to grow, with an increase in ablation time. Since the light will have a high refraction, the samples' reflection will also increase [14]. The figure reveals that the refractive index of $CuFeS_2$ NPs decreases as the photon wavelength increases in the visible region. The extinction coefficient shows the amount of energy lost due to molecules and other particles in the material scattering or absorbing light. Fig. 9**(b)** illustrates how the extinction coefficient varies with the incident light wavelength. It is evident that, when the ablation duration increases, the extinction coefficient rises for all prepared samples.

3.2.4. Skin depth, optical dielectric, and optical conductivity properties

Key factors related to photon absorption by nanoparticles are skin depth and optical conductivity. From the material's surface to its inside, the photon density drops exponentially because of a variety of factors, including the material density, surface shape, and refractive index. The absorption coefficient's inverse can be used to determine the skin depth ($\boldsymbol{\delta}$) [37].

$$\delta = \frac{1}{\alpha} \tag{9}$$

Fig. 9 demonstrates how the skin depth for $CuFeS_2$ NPs changes with photon energy at various ablation times.

The skin depth of $CuFeS_2$ NPs increases with an increase in photon energy. The band structure of the material is influenced by the optical

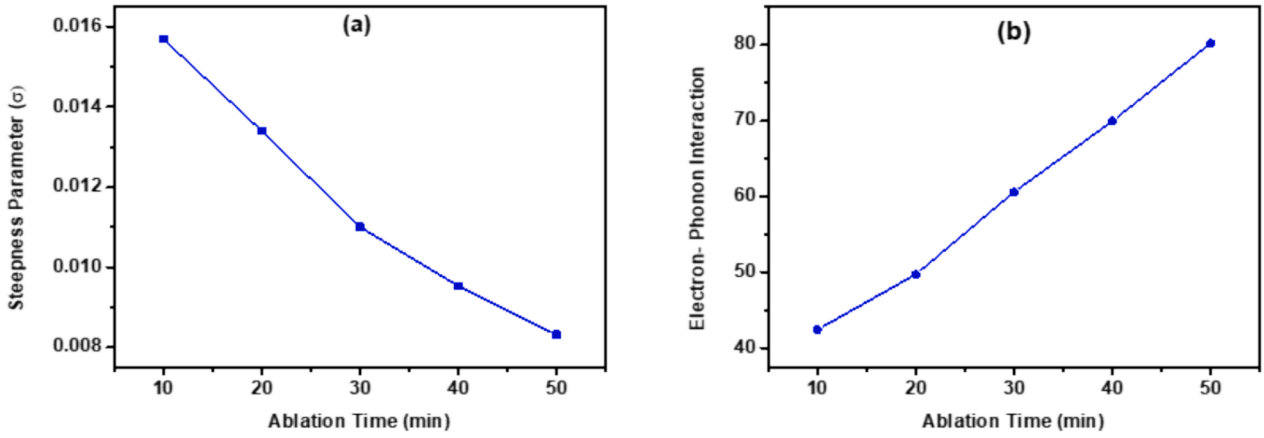

Fig. 7. The variation of both (a) the steepness parameter and (b) the electron–phonon interaction with the ablation time.

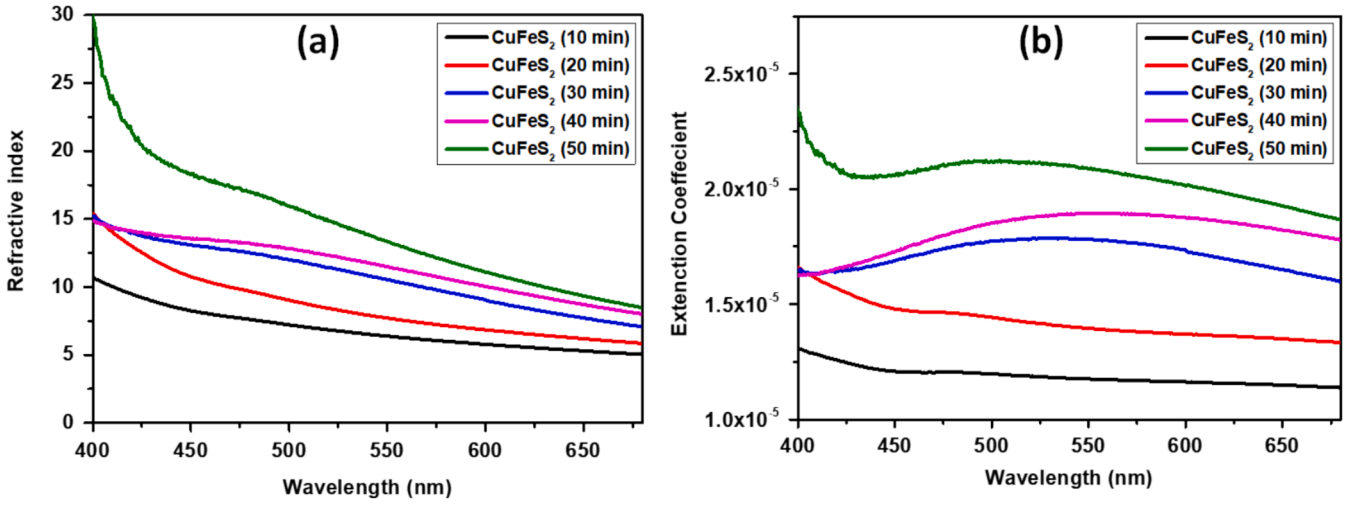

Fig. 8. (a) Refractive index; (b) Extinction coefficient for $CuFeS_2$ NPs samples at different ablation times.

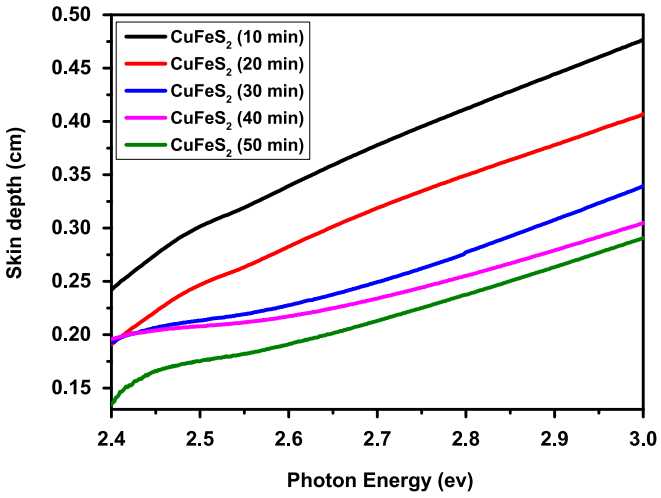

Fig. 9. Skin depth for $CuFeS_2$ NPs samples at different ablation times.

dielectric characteristics, which are linked to the energy density of states from within the optical bandgap of the samples. In materials, the optical dielectric loss (ε″) shows how much energy is taken in by an electric field when dipoles move, and the optical dielectric constant (ε′) shows how fast light is moving through the material [38,39]. The refractive index and extinction coefficient data can be used to compute the ε′ and ε″ using the following relations:

$$\varepsilon' = n^2 - k^2 \tag{10}$$

$$\varepsilon'' = 2nk \tag{11}$$

Fig. 10 displays the real and imaginary components of the dielectric constants as a function of input photon energy. As shown in Fig. 10**(a)**, the ε′ value increases with the increase in ablation time and incident photon energy. On the other hand, the value ε″ increases with the increase in the incident photon energy, as shown in Fig. 10**(b)**. The ε″ value increases from 0.0002 to 0.001 with an increase in ablation time. The rise in **n** and **k** values is correlated with the rise in ε′ and ε″ values.

When electrons are excited by an electromagnetic photon beam, which results in the migration of free charge carriers, optical conductivity (σ_{opt}) is produced [33]. The following equation describes how optical conductivity depends on the refractive index and absorption coefficient [34].

$$\sigma_{opt} = \alpha nc/4\pi \tag{12}$$

where **c** is the speed of light in vacuum ($c = 3 \times 10^8 m/sec$). Fig. 11**(a)** illustrates the relationship between the optical conductivity and the photon energy of $CuFeS_2$ NPs.

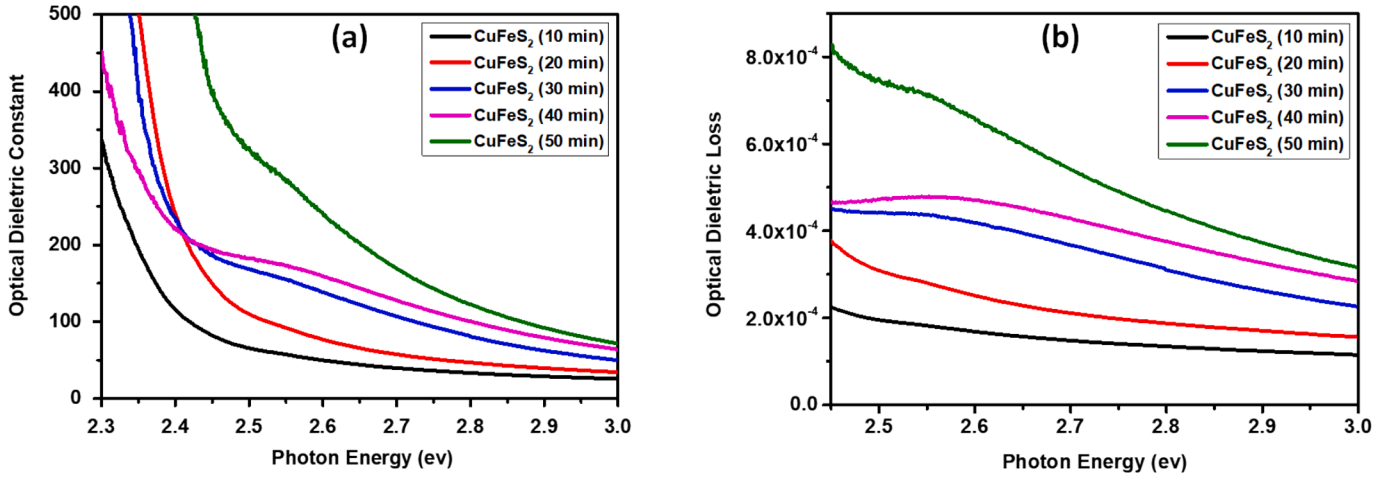

Fig. 10. (a) optical dielectric loss; (b) optical dielectric constant for $CuFeS_2$ NPs at different ablation times.

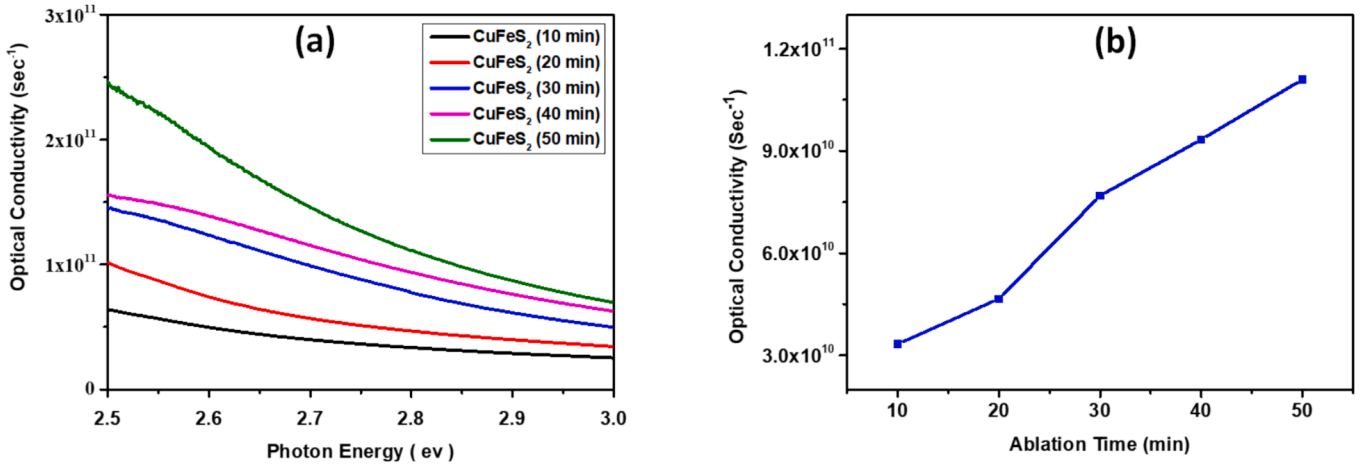

Fig. 11. (a) Optical conductivity with photon energy; (b) Optical conductivity variation with ablation time for $CuFeS_2$ NPs.

In the ultraviolet area, the optical conductivity rises in proportion to photon energy, which raises the number of free carriers. The higher energy area (UV absorption) is where optical conductivity increases the most, showing that free carriers of photon energy are available. This region also records the highest optical conductivity. However, free carrier trapping has significantly decreased the optical conductivity in the visible region [35]. Fig. 11**(b)** shows that the optical conductivity increased as the particle size of the $CuFeS_2$ NPs in ethanol increased.

4. Conclusion

We prepared $CuFeS_2$ NPs using a pulsed laser ablation technique in ethanol. We kept the laser energy at 480 mJ/pulse and the wavelength at 1064 nm throughout the ablation times of 10, 20, 30, 40, and 50 min. The TEM results showed that most nanoparticles in all samples are spherical, with average particle sizes ranging from 17.9 to 44.3 nm as the ablation time increased from 10 to 50 min. EDX measurements determine the influence of ablation time on the elemental compositions of Cu, S, and Fe. Using Raman spectroscopy, we found that the $CuFeS_2$ NPs have characteristic peaks at 275 cm^{-1}, 473 cm^{-1}, and 385 cm^{-1}. These peaks correspond to Cu—S bonds and Fe—S bonds, respectively. We attribute the O—H bending in FTIR analysis for $CuFeS_2$ NPs to their preparation in ethanol. We systematically analyzed the optical properties of $CuFeS_2$ NPs using UV–Vis spectra. The read shift of the absorption edges as the ablation time increases is due to the quantum confinement effect. The calculated values of the direct band gap ($\mathbf{E_g}$) decreased from 2.54 to 1.91 eV, while the value of the band tail energy ($\mathbf{E_u}$) increased from 1.64 to 3.11 eV by increasing the ablation time. The steepness parameter values decreased from 0.0157 to 0.00831, while the electron–phonon interaction values increased from 42.46 to 80.22, demonstrating an inverse proportionality. Furthermore, an increase in the ablation time reveals an increase in the values of the refractive index, dielectric constant, and optical conductivity.

CRediT authorship contribution statement

R. Onsi: Writing – review & editing, Writing – original draft, Methodology, Investigation, Formal analysis, Data curation, Conceptualization. **M. Nabil:** Writing – review & editing, Writing – original draft, Methodology, Investigation, Formal analysis, Data curation, Conceptualization. **S. Abdallah:** Writing – review & editing, Writing – original draft. **S. Negm:** Writing – original draft, Writing – review & editing. **k. Easawi:** Writing – review & editing, Writing – original draft, Investigation.

Declaration of competing interest

The authors declare that they have no known competing financial interests or personal relationships that could have appeared to influence the work reported in this paper.

Data availability

No data was used for the research described in the article.

References

[1] S. Sahoo, P. Pazhamalai, V.K. Mariappan, G.K. Veerasubramani, N.J. Kim, S.J. Kim, Hydrothermally synthesized chalcopyrite platelets as an electrode material for symmetric supercapacitors, Inorg. Chem. Front. 7 (7) (2020) 1492–1502, https://doi.org/10.1039/c9qi01335k.
[2] H. E. Nsude et al., "Green synthesis of CuFeS2 nanoparticles using mimosa leaves extract for photocatalysis and supercapacitor applications," J. Nanoparticle Res., vol. 22, no. 11, 2020, doi: 10.1007/s11051-020-05071-7.
[3] G. Sun et al., "Rational design and synthesis of nanosheets self-assembled hierarchical flower-ball-like CuFeS2 for boosted wide temperature sodium-ion batteries," Nano Res., vol. 16, no. 7, 2023, doi: 10.1007/s12274-023-5614-1.
[4] K. Yang, et al., Peracetic acid activation by natural chalcopyrite for metronidazole degradation: unveiling the effects of Cu-Fe bimetallic sites and sulfur species, Sep. Purif. Technol. 305 (2023), https://doi.org/10.1016/j.seppur.2022.122500.
[5] N. Tsogbadrakh, N. Jargalan, B. Batgerel, K. Tsookhuu, Electronic Structure, Magnetism and Magnetocrystalline Anisotropy of Antiferromagnetic Semiconducting Chalcopyrite, Defect Diffus. Forum 423 (2023), https://doi.org/10.4028/p-vah911.
[6] Z. Ding, C. Yang, H. Zhang, J. Mei, J. Wang, S. Yang, New utilizations of natural CuFeS2 as the raw material of Cu smelting for recovering Hg0 from Cu smelting flue gas, Fuel 341 (2023), https://doi.org/10.1016/j.fuel.2022.126997.
[7] B. Bhattacharyya, A. Pandey, CuFeS2 quantum dots and highly luminescent CuFeS2 based core/shell structures: synthesis, tunability, and photophysics, J. Am. Chem. Soc. 138 (32) (2016) 10207–10213, https://doi.org/10.1021/jacs.6b04981.
[8] M. Jomaa et al., "Structure and Optical Properties of LixAg1-xGaSe2 and LixAg1-xInSe2," Inorg. Chem., vol. 62, no. 19, 2023, doi: 10.1021/acs.inorgchem.3c00786.
[9] R.M. Obodo, et al., Annealing optimization of graphitized Co3O4@CuO@NiO composite electrodes for supercapacitor applications, Energy Storage 4 (5) (2022) 1–11, https://doi.org/10.1002/est2.347.
[10] R.M. Obodo, et al., Effects of copper ion irradiation on CuyZn1-2y-xMny/ GO supercapacitive electrodes, J. Appl. Electrochem. 51 (5) (2021) 829–845, https://doi.org/10.1007/s10800-021-01543-3.
[11] R.M. Obodo, et al., Exploring dual synergistic effects of CeO2@ZnO mediated sarcophrynium brachystachys leaf extract nanoparticles for supercapacitor electrodes applications, Hybrid Adv. vol. 5, no. January (2024) 100143, https://doi.org/10.1016/j.hybadv.2024.100143.
[12] R. M. Obodo et al., "Optimization of MnO2, NiO and MnO2@NiO electrodes using graphene oxide for supercapacitor applications," Curr. Res. Green Sustain. Chem., vol. 5, no. October, 2022, doi: 10.1016/j.crgsc.2022.100345.
[13] A. Alshoaibi, et al., Investigation of chemical bath deposited transition metals/GO nanocomposites for supercapacitive electrodes, Crystals 12 (11) (2022) 1–15, https://doi.org/10.3390/cryst12111613.
[14] S. Conejeros, P. Alemany, M. Llunell, I.D.P.R. Moreira, V. Sánchez, J. Llanos, Electronic structure and magnetic properties of CuFeS2, Inorg. Chem. 54 (10) (2015) 4840–4849, https://doi.org/10.1021/acs.inorgchem.5b00399.

[15] W. Ding, X. Wang, H. Peng, L. Hu, Electrochemical performance of the chalcopyrite CuFeS 2 as cathode for lithium ion battery, Mater. Chem. Phys. 137 (3) (2013) 872–876, https://doi.org/10.1016/j.matchemphys.2012.09.072.
[16] P. Rupa Ranjani, P. M. Anjana, and R. B. Rakhi, "Solvothermal synthesis of CuFeS2 nanoflakes as a promising electrode material for supercapacitors," J. Energy Storage, vol. 33, no. August 2020, p. 102063, 2021, doi: 10.1016/j.est.2020.102063.
[17] Y. Shao et al., "Mechanisms of the effect of sodium carbonate on the dispersion behavior of chalcopyrite and molybdenite," Zhongguo Kuangye Daxue Xuebao/Journal China Univ. Min. Technol., vol. 52, no. 2, 2023, doi: 10.13247/j.cnki.jcumt.20210742.
[18] D.J. Nangali, et al., Bioleaching of chalcopyrite using native Acidithiobacillus ferrooxidans isolated in a mining area in Kitwe Zambia, Sci. African 22 (2023), https://doi.org/10.1016/j.sciaf.2023.e01882.
[19] H. Nsude, et al., Binder-free fabricated CuFeS 2 electrodes for supercapacitor applications, Mater. Res. Express 9 (2022), https://doi.org/10.1088/2053-1591/ac4f13.
[20] S.A. Chang, P.Y. Wen, T. Wu, Y.W. Lin, Microwave-assisted synthesis of chalcopyrite/silver phosphate composites with enhanced degradation of rhodamine b under photo-fenton process, Nanomaterials 10 (11) (2020) 1–26, https://doi.org/10.3390/nano10112300.
[21] Z. Rdzawski, S. J, and W. Głuchowski, "Structure and properties of CuFe2 alloy," J. Achiev. Mater. Manuf. Eng., vol. 33, Mar. 2009.
[22] E. Fazio, et al., Nanoparticles engineering by pulsed laser ablation in liquids: concepts and applications, Nanomaterials 10 (11) (2020) 1–50, https://doi.org/10.3390/nano10112317.
[23] C.G. Moura, et al., Effects of laser fluence and liquid media on preparation of small Ag nanoparticles by laser ablation in liquid, Opt. Laser Technol. 97 (2017) 20–28, https://doi.org/10.1016/j.optlastec.2017.06.007.
[24] R. Onsi, K. Easawi, S. Abdallah, S. Negm, and H. Talaat, "Preparation of Silver Nanoparticles Dispersed in Almond Oil Using Laser Ablation Technique," in IOP Conference Series: Materials Science and Engineering, 2020, vol. 762, no. 1. doi: 10.1088/1757-899X/762/1/012005.
[25] M. Alheshibri, et al., Synthesis of Ag nanoparticles-decorated on CNTs/TiO2 nanocomposite as efficient photocatalysts via nanosecond pulsed laser ablation, Opt. Laser Technol. 155 (2022) 108443, https://doi.org/10.1016/j.optlastec.2022.108443.
[26] A. Al-Otaibi, et al., Pulsed laser ablation-mediated facile fabrication of MoO 3 /TiO 2 /rGO nanocomposite as a photocatalyst for dye degradation, Opt. Laser Technol. 170 (2024) 110156, https://doi.org/10.1016/j.optlastec.2023.110156.
[27] Z. Huang, et al., Manufacture of TiO 2 nanoparticles with high preparation efficiency and photocatalytic performance by controlling the parameters of pulsed laser ablation in liquid, Opt. Express 30 (12) (2022) 20482, https://doi.org/10.1364/oe.455658.
[28] H. Yu, et al., Synthesis and characterization of CuFeS2 and Se doped CuFeS2−xSex nanoparticles, J. Mater. Sci. Mater. Electron. 30 (13) (2019) 12269–12274, https://doi.org/10.1007/s10854-019-01586-5.
[29] N.R. Dhineshbabu, V. Rajendran, N. Nithyavathy, R. Vetumperumal, Study of structural and optical properties of cupric oxide nanoparticles, Appl. Nanosci. 6 (6) (2016) 933–939, https://doi.org/10.1007/s13204-015-0499-2.
[30] M. Nabil, S. Fouad, K. Easawi, S. Abdallah, Novel correlations between optical absorption and water desalination of Ag/Fe 3 O 4 nanocomposite prepared by pulsed laser ablation in liquid, Opt. Laser Technol. 164 (2023) 109545, https://doi.org/10.1016/j.optlastec.2023.109545.
[31] A.I. Abdel-salam, M.M. Awad, T.S. Soliman, A. Khalid, The effect of graphene on structure and optical properties of CdSe nanoparticles for optoelectronic application, J. Alloys Compd. 898 (2022) 162946, https://doi.org/10.1016/j.jallcom.2021.162946.
[32] A.S. Hassanien, A.A. Akl, Mechanochemical synthesis, structural, magnetic, optical and electrooptical properties of CuFeS2 nanoparticles, Appl. Phys. A Mater. Sci. Process. 124 (11) (2018) 1–16, https://doi.org/10.1007/s00339-018-2180-6.
[33] A.S. Hassanien, A.A. Akl, Effect of Se addition on optical and electrical properties of chalcogenide CdSSe thin films, Superlattices Microstruct. 89 (January) (2016) 153–169, https://doi.org/10.1016/j.spmi.2015.10.044.
[34] S. Fouad, et al., Assessing, surface morphology, optical, and electrical performance of ZnO thin film using ALD technique, J. Nanoparticle Res. 25 (2023), https://doi.org/10.1007/s11051-023-05816-0.
[35] S. S. Fouad, K. Easawi, T. Mahmoud, and M. Nabil, "Essential tips for enhancing the opto-electrical performance of CdSe (NPs)/Epoxy resin," J. Non. Cryst. Solids, 2023, [Online]. Available: https://api.semanticscholar.org/CorpusID:257288209.
[36] F. Horia, K. Easawi, R. Khalil, S. Abdallah, M. El-Mansy, S. Negm, Optical and thermophysical characterization of Fe3O4nanoparticle, IOP Conf. Ser. Mater. Sci. Eng. 956 (1) (2020), https://doi.org/10.1088/1757-899X/956/1/012016.
[37] A.S. Hassanien, A. Akl, Influence of composition on optical and dispersion parameters of thermally evaporated non-crystalline Cd50 S50-xSex thin films, J. Alloys Compd. 648 (2015) 280–290, https://doi.org/10.1016/j.jallcom.2015.06.231.
[38] T.S. Soliman, S.A. Vshivkov, S.I. Elkalashy, Structural , linear and nonlinear optical properties of Ni nanoparticles – Polyvinyl alcohol nanocomposite films for optoelectronic applications, Opt. Mater. (amst) vol. 107, no. April (2020) 110037, https://doi.org/10.1016/j.optmat.2020.110037.
[39] S. Fouad, B. Parditka, A. Bekheet, H. Atyia, Z. Erdelyi, ALD of TiO2/ZnO mutilayers towards the understanding of optical properties and polarizability, Opt. Laser Technol. 140 (2021) 107035, https://doi.org/10.1016/j.optlastec.2021.107035.